CrossMark

ORIGINAL ARTICLE

Mapping the Information Trace in Local Field Potentials by a Computational Method of Two-Dimensional Time-Shifting Synchronization Likelihood Based on Graphic Processing Unit Acceleration

Zi-Fang Zhao[1] · Xue-Zhu Li[1] · You Wan[1,2,3]

Abstract The local field potential (LFP) is a signal reflecting the electrical activity of neurons surrounding the electrode tip. Synchronization between LFP signals provides important details about how neural networks are organized. Synchronization between two distant brain regions is hard to detect using linear synchronization algorithms like correlation and coherence. Synchronization likelihood (SL) is a non-linear synchronization-detecting algorithm widely used in studies of neural signals from two distant brain areas. One drawback of non-linear algorithms is the heavy computational burden. In the present study, we proposed a graphic processing unit (GPU)-accelerated implementation of an SL algorithm with optional 2-dimensional time-shifting. We tested the algorithm with both artificial data and raw LFP data. The results showed that this method revealed detailed information from original data with the synchronization values of two temporal axes, delay time and onset time, and thus can be used to reconstruct the temporal structure of a neural network. Our results suggest that this GPU-accelerated method can be extended to other algorithms for processing time-series signals (like EEG and fMRI) using similar recording techniques.

✉ You Wan
    ywan@hsc.pku.edu.cn

1   Neuroscience Research Institute, Peking University, Beijing 100191, China

2   Department of Neurobiology, School of Basic Medical Sciences, Peking University, Beijing 100191, China

3   Key Laboratory for Neuroscience, Ministry of Education/ National Health and Family Planning Commission, Peking University, Beijing 100191, China

Introduction

An LFP is a summation of several neuronal assemblies and it is often hard to trace the corresponding sources [1–3]. Synchronized neural activity reveals important evidence about the information flow in neuronal networks [4, 5]. To detect the correlated oscillatory activity underlying LFPs in different brain regions, several algorithms have been developed. Classical linear synchronization detection algorithms are widely adopted but they are sensitive to phase-jitter [6–8]. Wide-band LFPs consist of nested oscillations [9]. Such oscillations always have a strict phase relationship reflecting how local neural assemblies are affected by external input [10]. Therefore, algorithms like amplitude-phase coherence and cross-correlation are very useful in this kind of application [6, 11]. Signals from two distant brain regions are generated by different cell assemblies and do not have a rigid phase-relationship [12]. Therefore, linear algorithms are not suitable for this type of application.

Synchronization likelihood (SL) was developed to analyze the synchronization between brain regions [13–15]. SL is an unbiased synchronization-detecting algorithm that compares the temporal patterns of two signals in terms of their time-delay embedding. This algorithm focuses more on the similarity between the temporal patterns of two signals and does not need a strict phase relationship between them. Therefore, SL algorithm is widely used in analyzing cross-regional LFP signals.

The typical synchronization detection method, including the original SL algorithm, usually does not consider the lag

654

Neurosci. Bull. December, 2017, 33(6):653–663

between LFPs in brain areas [15, 16]. A major reason for this is the great usage of computation time introduced by the extra time-shifting steps. Since different cell assemblies may not respond to an external stimulus simultaneously [17–20], it is better to take inter-regional delay into consideration. Accordingly, a methodology or an algorithm should consider the time required for information to pass from one brain region to another, to maximize the detecting sensitivity [18, 21]. We can calculate the synchronization relationship between two signals by adding an extra delay between them. Neural assemblies exhibit oscillatory activities with short epochs, and temporally sliding windows are also essential in finding the synchronized activities between two neural assemblies. It has been proposed that the lag between bi-directionally connected brain area like the hippocampus and medial pre-frontal cortex can be evaluated with linear amplitude cross-correlation methodology [6]. The SL algorithm has better performance in detecting non-stationary data and non-linear interdependence between distant brain regions [15]. However, the SL algorithm is very computationally intense and extra time-shifting iterations add significant time-consumption, which make it hardly applicable.

Recently, graphic processing unit (GPU) acceleration may enable the processing of massive amounts of experimental data within limited time and resources [22, 23]. Super-computing may now be possible with a desktop computer equipped with a high-end GPU [24]. Numerous solutions have been proposed recently for improving the speed of algorithms like cross-correlation with GPU super-computing [25].

In the present study, we propose a GPU-accelerated SL algorithm with 2-D time-shifting. We tested whether this method could reveal detailed information from original data with the synchronization values of two temporal axes, delay time and onset time, and thus if it can be used to reconstruct the temporal structure of a neural network.

Materials and Methods

Animal Surgery and Behavioral Experiment

Adult male Sprague-Dawley rats were used to record LFPs. They were provided by Department of Laboratory Animal Sciences, Peking University Health Science Center. All experiments were carried out following the Guidelines of the Animal Care and Use Committee of Peking University. Rats were housed individually with free access to food and water under a 12-h dark-light cycle. Thirteen rats weighing around 300 g were anesthetized using 1% sodium pentobarbital (0.5 mL/kg) and the head stabilized on a stereotaxic apparatus (David Kopf Instruments, Tujunga, CA).

When the animal did not respond to a pinch of the hind paw and a mild eyelid stimulus, the head skin was removed to expose the skull. The coordinates of regions of interest were determined as follows (in mm): anterior cingulate cortex (ACC), anterior/posterior (A/P) +2.3, medial/lateral (M/L) +0.7, dorsal/ventral (D/V) −2.2; primary somatosensory area 1 (S1), A/P −1.1, M/L −2.6, D/V −2.0. Six stainless screws were fixed to the skull without harming any brain tissues. These screws were also used for later stabilization of electrodes as well as the ground. Small craniotomies at the 4 sites with marked coordinates were carried out to expose the brain. Recordings were made from 2×4 rectangular micro-wire electrodes, each array 25-μm in diameter. Each electrode was implanted extremely slowly to the exact depth to avoid passing over the target tissue. All electrodes were glued to nearby screws using dental cement and vulnerable parts of the electrodes were also sealed in dental cement. Anesthesia was maintained with sodium pentobarbital during the whole procedure. After surgery, each rat was housed individually in its home cage for one week for recovery.

The chamber for behavioral experiments was made of transparent plastic and the floor was a grid plate with stainless steel bars. After getting accustomed to the chamber, the rat was allowed to move freely and monitored with a camera. A head stage was connected to the electrode during recording sessions. Laser stimulation was applied when the rat was lying quietly but not asleep. The laser beam was emitted from an ultra-pulse carbon dioxide laser therapeutic machine, with 2 cm from the tip of the laser guide arm to the rat's hind paw. The target spot was on the plantar surface of the left hind paw, with a slight shift from trial to trial to avoid heat damage. Noxious laser stimulation was provided using the continuous wave mode at 8–12 W for 30 ms. The exact power was adjusted according to paw-withdrawal behavior in each rat (power adjusted to 80% of that required to trigger behavior). Each session was carried out with 20 valid stimuli with an inter-stimulus interval of >60 s, and the time stamp of laser emission was recorded simultaneously. Each rat went through 4 sessions of laser stimulation with 2-day intervals between sessions.

Data Acquisition

We used a multi-channel recording system provided by Blackrock Microsystems Ltd (Salt Lake City, UT). LFP signals from the implanted electrodes were transferred through an analog band-pass filter (0.3 Hz–7.5 kHz) into digital form to reach the neural signal processor. Signals were sorted and recorded using Cerebus® software named "Central", also provided by Blackrock Microsystems Ltd. The digital filter was set with a pass band between 0 and 0.5 kHz with the sampling rate of 1 kS/s for LFP recording.

After each recording session, the recorded data were exported to MatLab (Mathworks, Natick, MA) through NeuroExplorer (Plexon, Dallas, TX).

Computer

We used a desktop computer with the setup i7 3930k CPU, 32GB RAM, NVidia GTX 560 GPU (with 384 CUDA cores, 2GB RAM, NVIDIA Corp., Santa Clara, CA), and another desktop computer with i7 2600 CPU, 16GB RAM, NVidia Tesla C2050 GPU (with 448 CUDA cores, 3GB RAM) to perform the computations.

Development of 2-Dimensional Time-Shift Correlation Algorithm

SL is a non-linear algorithm for synchronization detection [15]. Parameters like computation window size used in this work were set based on previously published work [14]. The workflow of the 2-D SL algorithm was as follows:

The first step was to select a temporal window for the synchronization detection in the first signal (source). This step was necessary because the onset of synchronized activities may occur in different brain sites at different times.

In the next step, a second temporal window was selected with a relative delay to the first temporal window. This window was then applied to the second signal (sink) to calculate the SL value between the source and the sink. The aim of this step was to find the delay of the synchronization from the source to the sink.

After calculating the SL value in all the time-shifting steps, we obtained an SL matrix with temporal resolution on both the delay axis and the time axis. With this extra delay axis, we evaluated synchronization events with a delay between two sites.

The 2-D time-shifting procedure increased the computing time markedly since the SL value needed to be calculated for many of the above two time-shifting steps. To solve this problem, we adopted a parallel computing technique with the GPU (explained later).

Data Processing

A flowchart of the whole synchronization matrix calculation is presented in Fig. 1A.

Data Pre-processing

The original signals were pre-processed in MatLab before the SL calculation. There were two main steps, re-sampling and filtering. The aim of re-sampling was to reduce the computational cost, and the filtering was to select the frequency band of interest. The filtering was based on a non-casual filter based on the fast-Fourier transform (FFT) and inverse FFT. The signal was first transformed into the frequency domain by FFT, unwanted frequency components were eliminated, and then an inverse FFT was applied to transform the signal back to the time domain. The parameters of these steps were based on the frequency band selected. Assuming that we selected low-pass (LP) and high-stop (HS) as the low- and high-frequency boundaries, the re-sampling rate was set to $3\times$ HS. Then a band pass filter was designed to filter the resampled data with a pass band from LP Hz to HS Hz.

GPU Acceleration in Synchronization Likelihood Matrix Calculation

The pre-processed signal was paired and sent to the SL calculation function (Fig. 1B). In this function, the synchronization values were calculated for a range of time-shifted computation windows of the two signals. The calculation mainly consisted of four steps.

First step was vectorization. Signals were sliced into non-overlapping vectors. The calculation ranges of vectors were selected from $-W_2$ to $-W_1$ and W_1 to W_2. And a reference vector was selected in the center of the signal. The purpose of W_1 was to avoid excess synchrony by the auto-correlation. W_2 was chosen based on the frequency of interest. Window width selection is shown in Equations 1 and 2 as previously reported [14]. fs is the sampling rate, LP is the low-pass frequency of the band-pass filter and p_{ref} is the probability that embedded vectors are "synchronized events" in the calculation window.

$$W_1 = 2 * fs/LP \tag{1}$$

$$n_{rec} = [W_2 - W_1 + 1] * p_{ref} \tag{2}$$

The second step was calculating the Euclidean distances between all vectors in the calculation window and the reference vector to evaluate each vector's similarity to the reference vector.

After calculating the Euclidean distance, for each channel, a hard threshold was set to select the 5% of vectors with the shortest Euclidean distances. These vectors were considered to be recurrent activities of the reference vector (Equation 2). This process is demonstrated in Fig. 1C. The temporal patterns of recurrent events in the two channels were compared. A simultaneously-occurring recurrent event was considered to be a synchronization event. The total number of synchronization events in the calculation window was calculated as shown in Equation 3.
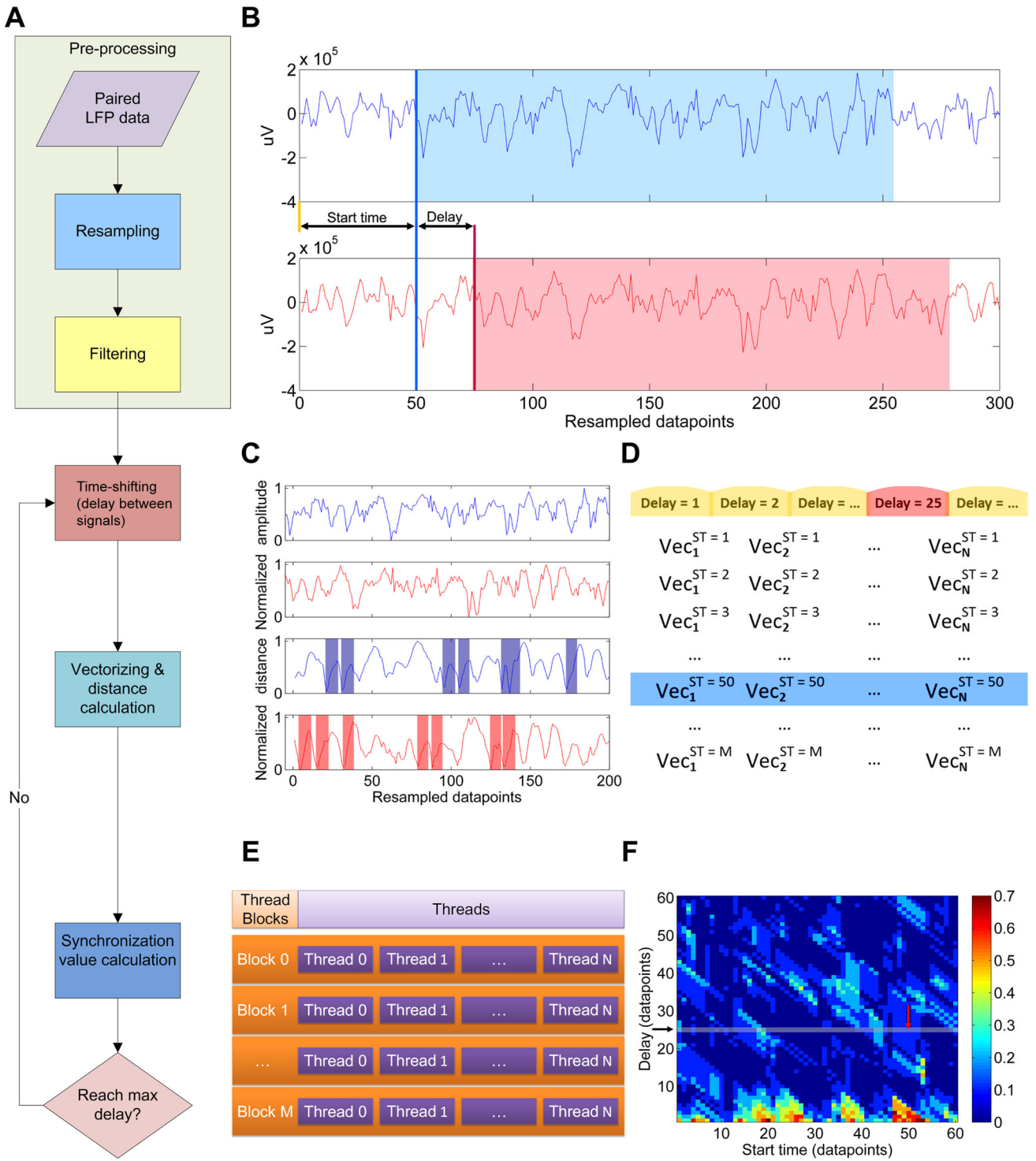
656

Neurosci. Bull. December, 2017, 33(6):653–663

A

Pre-processing

Paired
LFP data

↓

Resampling

↓

Filtering

↓

Time-shifting
(delay between
signals)

↓

Vectorizing &
distance
calculation

↓

Synchronization
value calculation

↓

Reach max
delay?

No

B

C

D

E

F

◄**Fig. 1** SL processing routine with GPU acceleration. **A** Flowchart of SL computing procedures. **B** Raw LFP traces from channel A (*blue*) and channel B (*red*). The SL calculating windows (*shaded*) are shifted by start time and delay from the beginnings of data segments. **C** The SL calculation process of a single computing step. *Upper two rows*: normalized LFP traces of selected time window; *lower two rows*: normalized Euclidean distance between each state vector and its reference vector in channel A (*blue*) and channel B (*red*). Shaded areas show the recurrent events in both channels. **D** Demonstration of SL calculating steps (Vec, vector; ST, start time). The current page is marked under the red tab to show a batch of parallel processing tasks simultaneously carried out by the GPU for the *red* data trace in **C** as time-shifting of 25 resampled data points at a delay. *Blue shaded* area in current page shows the parallel processing task carried out by the GPU for the *blue* data trace in **C** with 50 resampled data points from the initial calculating start point. **E** Task assignment for the GPU acceleration procedure. Each block is assigned to execute parallel processing tasks of a same start time. Every thread within a block is assigned to calculate the Euclidean distance between a state vector and its reference vector. For the same value in delay, all threads work simultaneously to cover all values in start time and therefore to realize GPU acceleration. **F** Synchronization matrix of LFP data of channels A and B. *Grey row* at a delay of 25 (*black arrow*) indicates the batch of parallel processing tasks shown in **D**. *Red arrow*, processing task shown within the *blue shaded* area in **D**.

$$n_{AB} = \sum_{j=i+w_2}^{i+w_1} n_j \tag{3}$$

The final step was SL value calculation. The synchronization value was calculated by dividing the number of synchronization events by the total number of recurrent events from both channels, as shown in Equation 4. After applying this calculation to different time-shifted signal pairs, we obtained a synchronization matrix (Fig. 1F).

$$SL_i = \frac{n_{AB}}{n_{rec}} \tag{4}$$

The GPU acceleration framework was developed into a custom CUDA mex-function. SL was calculated in parallel by the NVIDIA GPUs. CUDA is a parallel computing platform which enables the NVIDIA GPU to run C programs. To maximize the calculation speed, we integrated the full 2-D time-shifting SL routine in the C function. To reduce the CPU–GPU memory transfer overhead, we coded the full SL routine in the GPU. Two data segments were sent to the GPU memory in the beginning. Then each GPU thread was assigned a reference time point in one of the signals. The Euclidean distance between all vectors and the corresponding assigned reference time points were calculated by each GPU thread. In the next step, distances were sorted and the 5% of vectors with the shortest distances were selected as recurrent events. In the final step, for a specific data point in the 2-D synchronization matrix, an SL was calculated by comparing the ratio of overlapping recurrent events between two signals with corresponding delay and start times calculated in the previous step. All these 3 steps were performed in parallel with CUDA. And the result was returned from the GPU to the CPU only after the SL calculation.

Cross-Correlation

To compare the current method to a classical synchronization algorithm, we also analyzed our data using cross-correlation. Cross-correlation is a linear synchronization estimation method and is still widely used in analyzing electrophysiology signals [6, 16, 26].

To estimate the synchrony between LFPs, 3 steps are needed as reported previously [6]. (1) Band-pass filtering: LFP data are first filtered to the frequency of interest, for the Hilbert-transform has a narrow band assumption. This step was included in the pre-processing. (2) Calculating the power envelope using the Hilbert-transform, which was computed using *hilbert* in MatLab. The absolute value of the output complex numbers was calculated as the power envelope. (3) Cross-correlation of the power envelope: Mean amplitudes were initially removed from the power envelopes, then cross-correlation between the power envelopes was computed using the MatLab function x*corr*. To make a fair comparison with 2-D SL, we also computed the cross-correlation using a similar 2-D time-shifting window with a length of W_1 as in SL computation.

Simulations with Artificial Signals

In order to validate the performance of the 2-D SL algorithm, artificial data were constructed to perform simulations. In the first simulation, a 200-ms Gaussian smoothed 20-Hz beta wave was added to two segments of a pink noise signal at 100 ms and 130 ms. The signal-to-noise ratio (SNR) was set to 1, 2, and 10 to test the synchronization detection with different levels of noise. The signal was first filtered to the 13 Hz–30 Hz range then down-sampled to 150 Hz. The calculation window was set to −100 ms to 500 ms, and the delay searching range was set to −200 ms to 200 ms. For the SL algorithm, $n_{rec} = 20$ and $p_{ref} = 0.1$ were used. Cross-correlation with the same temporal range was calculated with a window of 50 ms. Ten simulations were conducted for each SNR level. Two sample *t* test was performed to test the synchronization significance within the synchronization event and outside the synchronization event.

To test the delay detection performance of the 2-D SL algorithm, a second testing dataset was constructed. An LFP epoch recorded from S1 was used as a signal template. Then this template was temporally shifted 30 ms to construct a delayed trace. Two levels of pink noise were added to both traces.

658

Neurosci. Bull. December, 2017, 33(6):653–663

Feature Extraction

In common electrophysiology experiments, we usually want to examine the neuronal activities in a particular circumstance, so we record the neuronal signals many times. For each trial, we may calculate the synchronization matrix for every pair of channels. Then we have a synchronization matrix with a size of subjects × trials × recording channel number^2 to deal with. Therefore, we need a suitable statistical method to further process these data.

The synchronization matrix shows the synchronization pattern between two recording channels. Our aim was to find the temporal pattern of synchronization and try to exclude the noise. Electrophysiological signals are not stationary, so we need to average all the synchronization events to summarize the stable synchronization pattern related to the experiment stimulus [15]. Our approach was to find the largest 5% of values in each synchronization matrix, and eliminate all small values under a threshold. The purpose of this procedure was to compress the data and find the strongest synchronization event in each trial, and to avoid introducing noisy synchronization events into the final result. After this step, each synchronization matrix was compressed into a few data points, and these data sets were easier to deal with.

Results

Test of 2-D Shifting Synchronization Likelihood

Two simulations were performed to test the performance of the 2-D SL algorithm in detecting synchronization between LFPs. In order to check the ability to detect transient synchronization between different recording areas with a propagation delay [21], the first simulation was set with a short epoch of delayed synchronization events. The raw waveforms of artificial LFP signals and the synchronization matrices of 2-D SL and cross-correlation are shown in Fig. 2A. Both algorithms failed to detect fine synchronization in a noisy situation; the *t* test indicated better detection by cross-correlation, as previously reported [6]. But the SL algorithm showed a clear relationship between the two signals in normal and high SNR situations, while the cross-correlation had more spurious correlations outside the synchronization event.

To further address the ability of the 2-D SL algorithm to reveal a driving relationship between two brain regions, a second simulation was performed. We calculated the LFP segment recorded from S1 with a 30-ms-delayed version of the same segment with low and high levels of pink noise added to both LFP traces. The results for the 2-D SL

algorithm, cross-correlation, and the synchronization value distribution in the delay axis are shown in Fig. 2B. The SL algorithm showed a much smoother distribution than the cross-correlation even in the low SNR situation while the cross-correlation shows many side peaks in the low SNR situation.

We also compared the calculation speed of 2-D SL (CPU version), 2-D SL (GPU version), and cross-correlation (Fig. 3). Because of the communication overheads of the GPU, the GPU version was slightly slower than the CPU version of SL and cross-correlation. As the computation blocks increased, the GPU version quickly overtook the other 2 algorithms and showed a slower increase in computing time. With 105 time-shifting operations, the GPU SL only took 367 ms, while cross-correlation took 17 s (46.3× acceleration) and the CPU SL took 55.2 s (151.1× acceleration) to finish the computation.

Extraction of Synchronization Events from Multichannel Electrode Recordings

After validation of the 2-D SL algorithm, we tested it on LFP data recorded from implanted electrodes from 13 awake, freely-moving rats. Each rat with 8-channel micro-wire electrodes in S1 and the ACC received laser stimulation. Whenever a noxious laser stimulus was applied to the left hind paw, nociceptive information passed through the central nervous system to reach S1 and the ACC for information integration [27]. Timing is very important in this process, because there are different components of pain perception and each passes through a different pathway to generate different aspects such as a tingling sensation and negative emotion [28].

Synchronization matrices around the noxious laser stimulus onset were calculated (Fig. 4). Both SL and cross-correlation detected fine 0-lag synchronization between a selected pair of recording electrodes in S1. SL had a narrower peak and lower background noise. Synchronization between a pair of electrodes in S1 and ACC had more noise. SL showed transient synchronizations from S1 to ACC with a positive delay before stimulation onset, while cross-correlation failed to detect this.

Constructing the Temporal Structure of the Neural Network

Using the synchronization matrices, we can define the temporal relationship between two recording sites. The detailed temporal synchronization relationship can be mapped using several synchronization matrices derived from more than 2 recording sites and in several frequency bands. The detailed temporal synchronization map can reveal the pattern of brain activity.
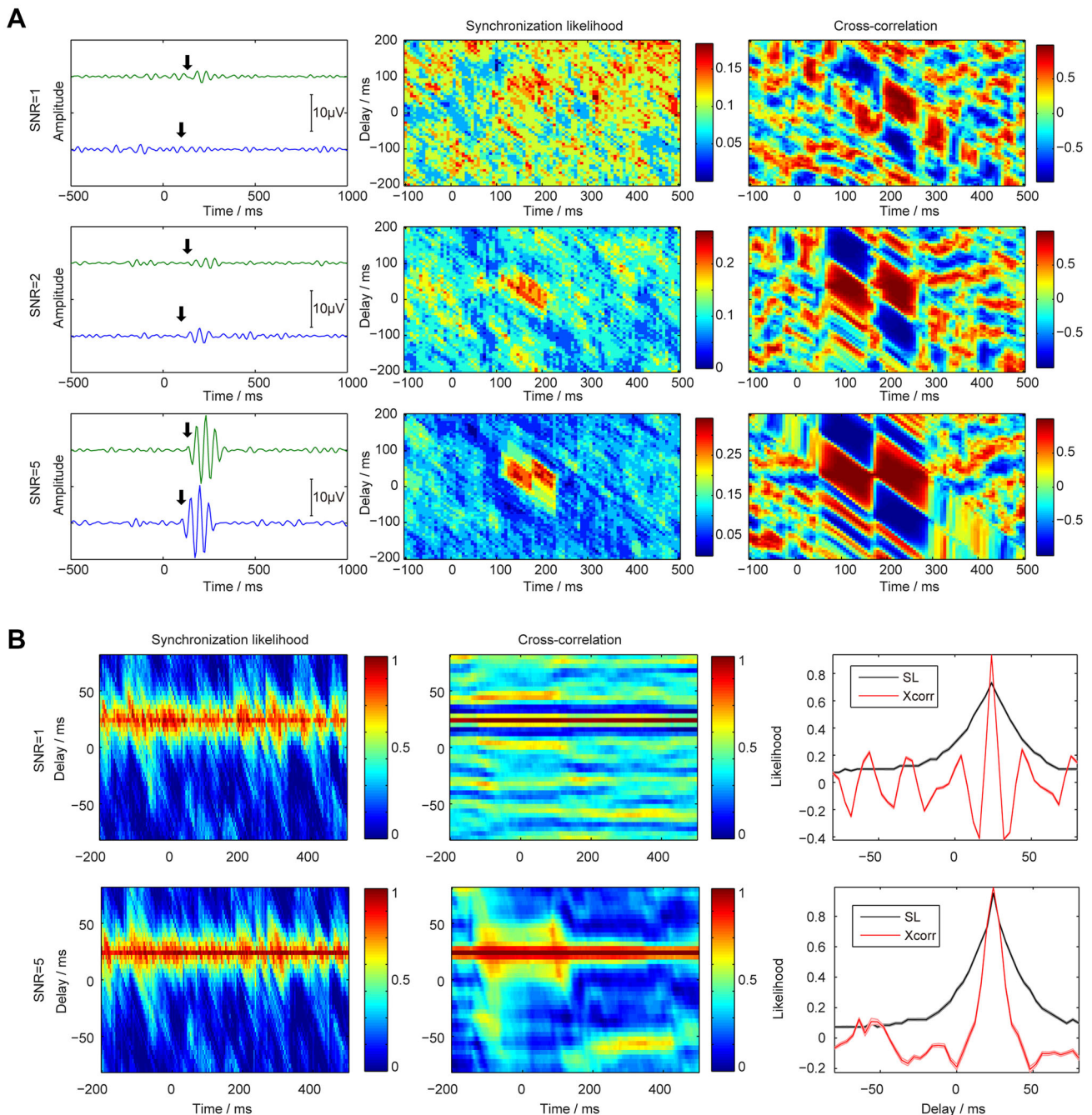
Fig. 2 Artificial signal validation using two simulation tasks. **A** Synchronization event detection using 2-D SL and cross-correlation. *Left panels*, test signal with different levels of pink noise and a short epoch of beta oscillation; middle panels, results of SL; *right panels*, result of cross-correlation. *Note* that the SL had a lower synchronization value than the cross-correlation outside the synchronization event. **B** Lag estimation between gamma-band LFP signal and a 30-ms delayed version with different levels of pink noise. *Note* that the SL always had a smoother distribution in the delay axis than cross-correlation, especially in the low SNR situation.

Noxious laser stimulation was used in the present study as a paradigm. Pain is a complex neural process that involves a "pain network" including many brain regions [28–30]. It is important to know how these brain regions are dynamically coupled during the onset of pain. Our method provides a powerful tool for studying the dynamics

of spatially separated brain regions. As our results demonstrated, the temporal synchronization relationship between the S1 and the ACC was more significant when a noxious laser stimulus was applied (Fig. 5). The sensory-discriminative aspect of nociceptive information passes through the thalamus to S1 in the lateral pain pathway [31, 32],
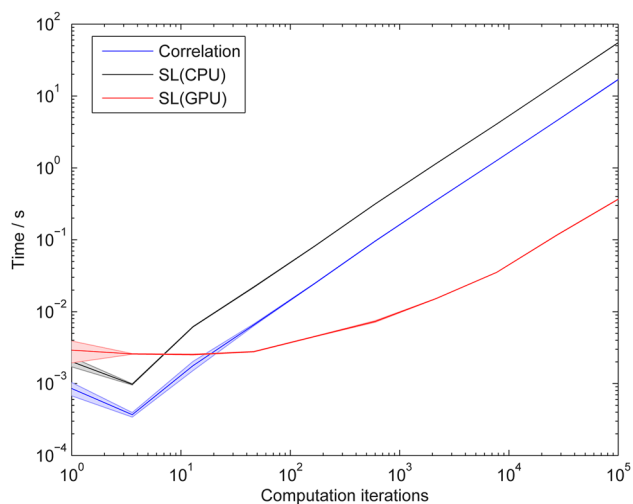
Fig. 3 Computation speed comparison. Time consumption for calculating different numbers of time-shifting steps for cross-correlation (*blue*), the CPU version of SL (*black*), and the GPU version of SL (*red*). Both the CPU version of SL and cross-correlation had a linear increase in calculation time with increasing numbers of calculation steps. The CPU version of SL was 4 times slower than cross-correlation. The GPU version of SL was slower with fewer calculation steps but yielded a $151\times$ increase in speed than the CPU version with many calculation steps. *Shaded areas*, standard error.
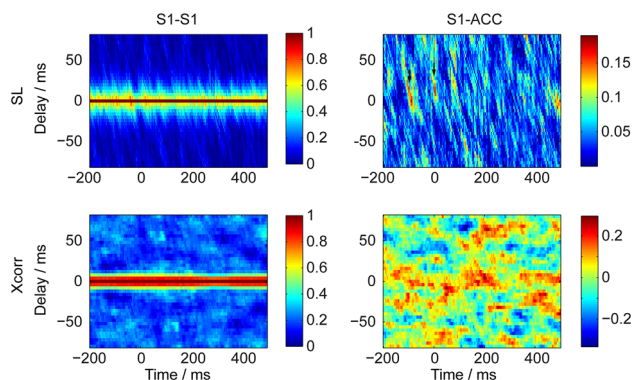

Fig. 4 Synchronization between S1 and ACC in the gamma band. Synchronization detection of a pair of recording sites within S1 and between S1 and ACC with 2-D SL and cross-correlation. Both algorithms detected a 0-phase lag correlation within S1. *Note* that SL had a cleaner background. SL detected transient epochs of synchronization between S1 and ACC with a positive lag (*black arrows*) while cross-correlation shows a result with more noise.

Fig. 5 Temporal synchronization maps of S1 and the ACC in different frequency bands (delta, theta, alpha, beta, and gamma). Each bin is the maximal SL value along the corresponding delay axis, and then normalized across the start time axis. **A** and **B** are representing maps of control group and noxious laser group, respectively.

while the affective-motivational aspect of this information also arrives at the thalamus and then passes through the medial pain pathway to the ACC [33–35]. Fibers between the S1 and the ACC have been tracked when both regions are activated during painful sensation in humans [36]. Their anatomical connections are mainly *via* fiber connections with the secondary somatosensory cortex and the insular cortex [37]. Thus, our results further confirm the
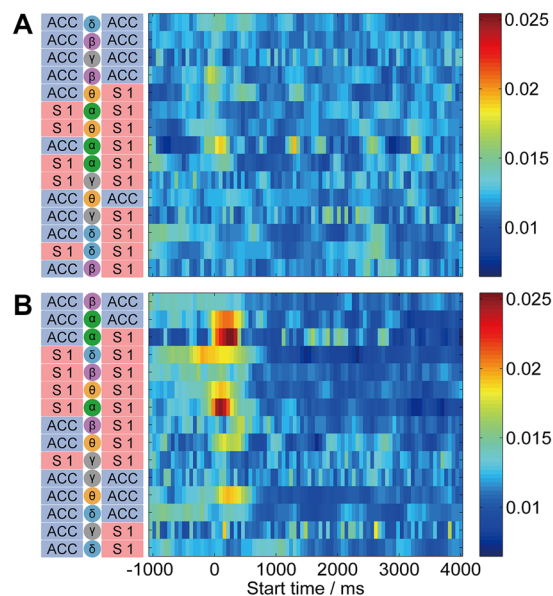
temporal synchronization relationship between S1 and the ACC during pain perception.

In the present study, we also arranged all synchronization events in temporal order to better visualize the data (Fig. 6). First, we compressed all synchronization matrices into 1-D arrays. This step was carried out by finding the maximum value along the delay-axis to represent the synchronization event occurring at every start time. The next step was sorting the 1-D arrays by temporal order. We assumed that event-related activities invoked synchronization between different pairs of brain regions at different time points. Thus, after sorting the 1-D arrays of different synchronization matrices, all arrays were merged into a final matrix in ascending order of the time of appearance of the synchronization maximum, providing trace varying with synchronization. To see the temporal pattern more clearly, the synchronization arrays were normalized. In this final matrix, we observed that some channel-pairs showed characterized temporal pattern with peaks in synchronization arrays rather than a uniform distribution. This map showed their maximum synchronization aligned in temporal order.

From this temporal pattern map, we visualized the flow of event-related information. Information in the delay axis was further analyzed to study the driving relationship between brain regions (Fig. 6). The data showed that in the delta and gamma bands, the SL values were biased to a positive delay while in the theta band the bias was to a negative delay. These results suggest that S1 precedes ACC
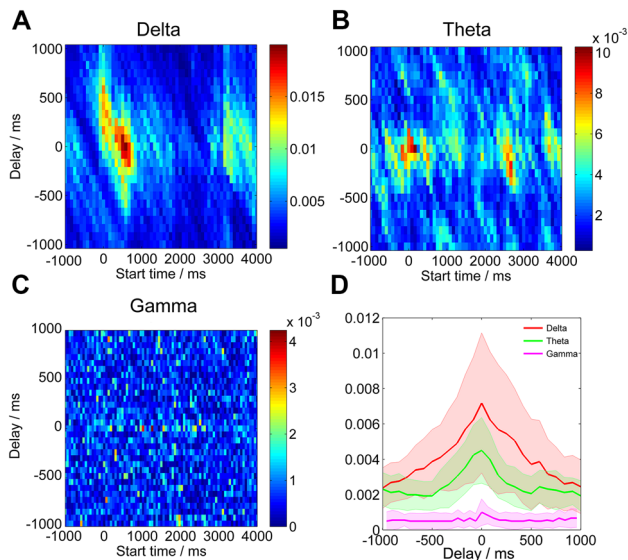
Fig. 6 SL matrices of S1 and the ACC in several frequency bands and their delay distribution values. **A–C** SL matrices demonstrating the temporal distribution of notable synchronization events cumulated from all channel pairs between S1 and the ACC in the delta (**A**), theta (**B**), and gamma bands (**C**). **D** SL value distribution along the delay axis from these three SL matrices (*red*, delta; *green*, theta; *purple*, gamma). At each step of delay, the SL values of all start times with the same delay were calculated for the median and standard deviation. Each solid line represents the median along the delay axis of each frequency band, and the shadowed area of the same color represents the standard deviation along the delay axis of that band.

in the delta and gamma bands, while the ACC tends to be activated earlier than S1.

Discussion

Our work established a novel method to analyze the dynamics of neural networks. By the 2-dimensional time-shifting approach, we managed to visualize the synchrony in activities between different brain areas with high temporal resolution. The parallel computing technique was integrated into our work to support the massive computation. This method was demonstrated to have a high accuracy in detecting the temporal characteristics of information flow in a neural network.

Evaluating the Direction of Information Transfer

For time-shifting synchronization detection algorithms, a delayed correlation peak may suggest a potential causality or driving relationship [38]. This idea is simple and straightforward, but it is always hard to perform this kind of computation for high-density electrophysiology because of the unrealistic computation time. With the GPU-

accelerated 2-D SL algorithm we developed, this type of analysis has become more feasible.

If two brain regions have mutual connections, the correlation may rise in both of the synchronization matrixes in a temporal order, and the matrix describing the initial innervating direction will show an earlier uptake. If the connection is unidirectional, only the matrix in the innervating direction shows a correlation uptake, and values from the matrices can reveal how much the two channels are reciprocally driven.

Kernel Algorithm Selection and Limitation

Our method was based on the SL algorithm. Technically, any algorithm that can detect synchronization or a correlation between two time-series can be the kernel algorithm for studying neural dynamics [39, 40]. Based on the characteristics of each algorithm, the corresponding analysis would be fit to solve different problems. We will not go through these algorithms in detail here, but they share a common weakness: the correlation or synchronization cannot prove causality [41, 42]. With current techniques, neurons of the central nervous system are sampled by a limited number of probes. This means that the number of sources is larger than the number of probes.

Whenever synchronization is detected between two sites, we can only infer that the activity of the latter is likely to be a response to the former. But we cannot exclude the possibility that synchronized activities of both sites may be the result of the activity of another site as a common source, while it takes different propagation times to get to the receiving sites. Our method was based on one of these algorithms, so it also has the same drawback. However, the 2-D time-shifting provided more information to verify the result. With this additional information, anatomical knowledge can be more easily incorporated into the data explanation. For example, we can use the distribution of delays as an indicator of the stability of information transfer. If the delay of synchronized activity is very stable, the lag-distribution would be narrow, and this would make the conclusion more convincing. Temporal order is another key clue for investigation. With results like those shown in Figs 4 and 5, anatomical knowledge can be included to explain the results.

Future Applications in Time-Series Signals

Our method was developed based on the LFP, which is a type of time-series signal. It is easy to extend this method to other multi-site time-series signals like magnetoencephalography (MEG), positron emission tomography (PET), and spiking multi-unit activity. All these types of data can use this framework to extract the synchronization

onsets and reconstruct the temporal pattern of activities between recording sites. Our present study suggests that this method could support better envisioning of neural network dynamics.

Compliance with Ethical Standards

Conflict of interest The authors declare no conflict of interests.

References

1. Gloor P. Neuronal generators and the problem of localization in electroencephalography: application of volume conductor theory to electroencephalography. J Clin Neurophysiol 1985, 2: 327–354.
2. Pascual-Marqui RD. Review of methods for solving the EEG inverse problem. Int J Bioelectromagn 1999, 1: 75–86.
3. Siebenhühner F, Lobier M, Wang SH, Palva S, Palva JM. Measuring large-scale synchronization with human MEG and EEG: challenges and solutions. In: Palva S (Ed.). Multimodal Oscillation-Based Connectivity Theory. Springer, 2016: 1–18.
4. Sirota A, Montgomery S, Fujisawa S, Isomura Y, Zugaro M, Buzsáki Gr. Entrainment of neocortical neurons and gamma oscillations by the hippocampal theta rhythm. Neuron 2008, 60: 683–697.
5. Yamamoto J, Suh J, Takeuchi D, Tonegawa S. Successful execution of working memory linked to synchronized high-frequency gamma oscillations. Cell 2014, 157: 845–857.
6. Adhikari A, Sigurdsson T, Topiwala MA, Gordon JA. Cross-correlation of instantaneous amplitudes of field potential oscillations: a straightforward method to estimate the directionality and lag between brain areas. J Neurosci Methods 2010, 191: 191–200.
7. Baria AT, Mansour A, Huang L, Baliki MN, Cecchi GA, Mesulam MM, et al. Linking human brain local activity fluctuations to structural and functional network architectures. NeuroImage 2013, 73: 144–155.
8. Kuo M-F, Nitsche MA. Exploring prefrontal cortex functions in healthy humans by transcranial electrical stimulation. Neurosci Bull 2015, 31: 198–206.
9. Buzsaki G, Mizuseki K. The log-dynamic brain: how skewed distributions affect network operations. Nat Rev Neurosci 2014, 15: 264–278.
10. Schomburg EW, Fernández-Ruiz A, Mizuseki K, Berényi A, Anastassiou CA, Koch C, et al. Theta phase segregation of input-specific gamma patterns in entorhinal-hippocampal networks. Neuron 2014, 84: 470–485.
11. Wang J, Li D, Li X, Liu FY, Xing GG, Cai J, et al. Phase-amplitude coupling between theta and gamma oscillations during nociception in rat electroencephalography. Neurosci Lett 2011, 499: 84–87.
12. Gareth B. Do sustained and long range zero-phase lag correlations develop in the human brain? Front Neurosci 2010, 4: 486–493.
13. Yu H, Liu J, Cai L, Wang J, Cao Y, Hao C. Functional brain networks in healthy subjects under acupuncture stimulation: an EEG study based on nonlinear synchronization likelihood analysis. Phys A Stat Mech Appl 2017, 468: 566–577.
14. Montez T, Linkenkaer-Hansen K, van Dijk BW, Stam CJ. Synchronization likelihood with explicit time-frequency priors. NeuroImage 2006, 33: 1117–1125.
15. Stam C, Van Dijk B. Synchronization likelihood: an unbiased measure of generalized synchronization in multivariate data sets. Phys D Nonlinear Phenom 2002, 163: 236–251.
16. Hipp JF, Hawellek DJ, Corbetta M, Siegel M, Engel AK. Large-scale cortical correlation structure of spontaneous oscillatory activity. Nat Neurosci 2012, 15: 884–890.
17. Kaplan R, Adhikari MH, Hindriks R, Mantini D, Murayama Y, Logothetis NK, et al. Hippocampal sharp-wave ripples influence selective activation of the default mode network. Curr Biol 2016, 26: 686–691.
18. Ramirez-Villegas JF, Logothetis NK, Besserve M. Diversity of sharp-wave-ripple LFP signatures reveals differentiated brain-wide dynamical events. Proc Natl Acad Sci U S A 2015, 112: E6379–E6387.
19. Gregoriou GG, Gotts SJ, Zhou H, Desimone R. High-frequency, long-range coupling between prefrontal and visual cortex during attention. Science 2009, 324: 1207–1210.
20. Salinas E, Sejnowski TJ. Correlated neuronal activity and the flow of neural information. Nat Rev Neurosci 2001, 2: 539–550.
21. Pijn JP, da Silva FL. Propagation of electrical activity: nonlinear associations and time delays between EEG signals. Basic Mech EEG 1993: 41–61.
22. Owens JD, Houston M, Luebke D, Green S, Stone JE, Phillips JC. GPU computing. Proc IEEE 2008, 96: 879–899.
23. Rossant C, Kadir SN, Goodman DF, Schulman J, Hunter ML, Saleem AB, et al. Spike sorting for large, dense electrode arrays. Nat Neurosci 2016, 19: 634–641.
24. Richert M, Nageswaran JM, Dutt N, Krichmar JL. An efficient simulation environment for modeling large-scale cortical processing. Front Neuroinform 2011, 5: 19.
25. Kapinchev K, Bradu A, Barnes F, Podoleanu A. GPU implementation of cross-correlation for image generation in real time. Int Conf Signal Process Commun Syst 2015: 1–6.
26. Buzsaki G, Wang XJ. Mechanisms of gamma oscillations. Annu Rev Neurosci 2012, 35: 203–225.
27. Eto K, Wake H, Watanabe M, Ishibashi H, Noda M, Yanagawa Y, et al. Inter-regional contribution of enhanced activity of the primary somatosensory cortex to the anterior cingulate cortex accelerates chronic pain behavior. J Neurosci 2011, 31: 7631–7636.
28. Ploner M, Sorg C, Gross J. Brain rhythms of pain. Trends Cognit Sci 2017, 21:100–110.
29. Ossipov MH, Dussor GO. Central modulation of pain. J Clin Investig 2010, 120: 3779–3787.
30. Tracey I, Johns E. The pain matrix: reloaded or reborn as we image tonic pain using arterial spin labelling. Pain 2010, 148: 359–360.
31. Chen LM, Dillenburger BC, Wang F, Friedman RM, Avison MJ. High-resolution functional magnetic resonance imaging mapping of noxious heat and tactile activations along the central sulcus in New World monkeys. Pain 2011, 152: 522–532.
32. Liu CC, Veldhuijzen DS, Ohara S, Winberry J, Greenspan DJ, Lenz AF. Spatial attention to thermal pain stimuli in subjects with visual spatial hemi-neglect: extinction, mislocalization and misidentification of stimulus modality. Pain 2011, 152: 498–506.
33. Diers M, Christmann C, Koeppe C, Ruf M, Flor H. Mirrored, imagined and executed movements differentially activate sensorimotor cortex in amputees with and without phantom limb pain. Pain 2010, 149: 296–304.
34. Yoshino A, Okamoto Y, Onoda K, Yoshimura S, Kunisato Y, Demoto Y, et al. Sadness enhances the experience of pain via neural activation in the anterior cingulate cortex and amygdala: an fMRI study. Neuroimage 2010, 50: 1194–1201.

35. Friebel U, Eickhoff SB, Lotze M. Coordinate-based meta-analysis of experimentally induced and chronic persistent neuropathic pain. Neuroimage 2011, 58: 1070–1080.

36. Moisset X, Bouhassira D. Brain imaging of neuropathic pain. Neuroimage 2007, 37: S80–S88.

37. Price DD. Psychological and neural mechanisms of the affective dimension of pain. Science 2000, 288: 1769.

38. Gersch W. Causality or driving in electrophysiological signal analysis. Math Biosci 1972, 14: 177–196.

39. Li X, Ouyang G. Estimating coupling direction between neuronal populations with permutation conditional mutual information. NeuroImage 2010, 52: 497–507.

40. Quiroga RQ, Kraskov A, Kreuz T, Grassberger P. Performance of different synchronization measures in real data: a case study on electroencephalographic signals. Phys Rev E Stat Nonlinear Soft Matter Phys 2005, 65: 041903.

41. Demariedreblow D. Relation between knowledge and memory: a reminder that correlation does not imply causality. Child Dev 1991, 62: 484–498.

42. Aldrich J. Correlations genuine and spurious in Pearson and Yule. Stat Sci 1995, 10: 364–376.